



RESEARCH ARTICLE | MARCH 12 2024

Effect of surface roughness on large-scale downburst-like impinging jets

Federico Canepa   ; Massimiliano Burlando  ; Djordje Romanic  ; Horia Hangan



Physics of Fluids 36, 036610 (2024)

<https://doi.org/10.1063/5.0198291>



View
Online



Export
Citation

CrossMark



Physics of Fluids

Special Topic: K. R. Sreenivasan:
A Tribute on the occasion of his 75th Birthday

[Submit Today](#)



Effect of surface roughness on large-scale downburst-like impinging jets

Cite as: Phys. Fluids **36**, 036610 (2024); doi: [10.1063/5.0198291](https://doi.org/10.1063/5.0198291)

Submitted: 17 January 2024 · Accepted: 24 February 2024 ·

Published Online: 12 March 2024



View Online



Export Citation



CrossMark

Federico Canepa,^{1,2,a)}  Massimiliano Burlando,¹  Djordje Romanic,^{2,3}  and Horia Hangan^{2,4}

AFFILIATIONS

¹Department of Civil, Chemical and Environmental Engineering (DICCA), Polytechnic School, University of Genoa, Via Montallegro 1, 16145 Genoa, Italy

²Wind Engineering, Energy and Environment (WindEEE) Research Institute, Western University, 2535 Advanced Avenue, London, Ontario N6M 0E2, Canada

³Department of Atmospheric and Oceanic Sciences, Faculty of Science, McGill University, Burnside Hall, 805 Sherbrook Street West, Montreal, Quebec H3A 0B9, Canada

⁴Faculty of Engineering and Applied Science, Ontario Tech University, 2000 Simcoe Street North, Oshawa, Ontario L1G 0C5, Canada

^{a)} Author to whom correspondence should be addressed: federico.canepa@unige.it

ABSTRACT

Downbursts are cold descending winds that develop from thunderstorm clouds and, after impingement on the ground, produce an intense low-level horizontal front characterized by an axisymmetric toroidal vortex structure. Surface roughness is a key factor in the characterization of mean and turbulent wind speed features of synoptic-scale stationary atmospheric boundary layer winds. The goal of the present research is to physically assess whether the same can apply to the surface layer produced during thunderstorms, which are non-stationary, highly time-transient, and spatially limited phenomena. Downburst-like flows were produced through the impinging jet technique at the WindEEE Dome, at Western University in Canada. Three different surfaces were tested, and an equivalent full-scale roughness length ($z_{0,eq}$) was determined. Experimental records are made publicly available. The large geometric and kinematic scales produced high Reynolds numbers, which enabled us to classify the flow as “fully turbulent” and therefore representative of full-scale downbursts. Results indicate a weak dependency on the Reynolds number, which suggests no relevant flaws in extending the results to the natural environment. The overall wind speed maxima weakly depend on z_0 , whereas a sharp velocity decrease is observed beyond the radial position of the maxima with increasing z_0 . Surface roughness enhances the boundary layer separation and consequently elevates the height of maximum wind speed above the surface. Vertical profiles of the horizontal velocity return a quite clear nose shape. Turbulence intensity shows a C-like shape with maxima in the near proximity of the ground that increase with z_0 .

© 2024 Author(s). All article content, except where otherwise noted, is licensed under a Creative Commons Attribution (CC BY) license (<http://creativecommons.org/licenses/by/4.0/>). <https://doi.org/10.1063/5.0198291>

I. INTRODUCTION

Forcing orographic uplifting mechanisms as well as microclimatic conditions, like the presence of warm and humid air near ground or sea levels, often foster the formation of convective updraft of air parcels that eventually form cumulonimbus clouds. Their vertical extent often reaches the top of the troposphere (at mid-latitudes, about 11 km on average above the sea level, ASL), and sometimes beyond with a typical anvil-shaped leak in the tropopause due to the updraft strength. No convective phenomena are measured in the upper stratosphere. The air parcels in the thunderstorm cloud, which after entraining environmental air that promotes evaporation and sublimation, are colder and denser with respect to the surrounding environment, buoyantly fall

from the cloud base toward the ground in the so-called downdraft. The instability between the descending column of cold air and the calm surrounding environment produces axisymmetric toroidal vortical structures, whose leading eddy is named primary vortex (PV). With the flow approaching the ground, the surface pressure augments while the flow momentum changes from vertical to horizontal (Canepa *et al.*, 2022b). It follows that the downdraft diverges into an intense horizontal outflow with ideal radial symmetry. Upon hitting the surface, the PV leads the outflow and produces maximum horizontal wind speeds between the center of the vortex and the surface level, producing a nose-shaped vertical profile (Junayed *et al.*, 2019 and Canepa *et al.*, 2020). Here, the velocity field is determined by the

balance between the PV forcing, i.e., superposition of internal rotational speed and advection velocity of the outward propagating vortex, and the no-slip boundary condition at the ground. The same holds for the smaller and weaker secondary vortical structures that follow the PV in space and time, i.e., the trailing vortices. According to this downburst model [see, for instance, [Byers and Braham \(1948\)](#)], the horizontal velocity signal of downbursts is non-stationary, as outlined by [Canepa et al. \(2022c\)](#) and later in Sec. IV. The real downburst outflows can present supplementary flow interactions. In addition to the PV forcing and no-slip condition, the real flow field is often affected by the translation of the parent cumulonimbus cloud as well as the background Atmospheric Boundary Layer (ABL) wind. A recent extensive large-scale experimental campaign assessed these interactions to deepen the characterization of the space and time evolution of the phenomenon in nature ([Romanic and Hangan, 2020](#) and [Canepa et al., 2022c; 2022b; 2022a](#)).

Another open question concerns the surface roughness. The exploration of surface roughness effects encompasses an extensive array of subjects, ranging from mechanical and thermodynamic issues such as fluid flow in pipes ([Farshad et al., 2001](#)) to chemical applications, for instance, the production of ozone ([Meyer et al., 2023](#)) or surface ionization waves ([Konina et al., 2022](#)). In wind engineering and for ABL flows, the surface roughness is commonly taken into account through the parameter named roughness length z_0 ([Davenport, 1963](#)): Is this quantity relevant to the transient dynamics of the thunderstorm outflow? Stationary and Gaussian ABL winds strongly depend on the surface roughness. z_0 alters the logarithmic vertical profile of the mean wind speed by increasing the height of the ABL top above the ground level (AGL). The turbulence intensity also increases considerably with z_0 at the near-ground level. It is therefore relevant to assess whether the same holds for thunderstorm winds and to which extent wind profiles are eventually affected by z_0 . Hereafter, we will address this question through the results of the large-scale experimental campaign that recently took place at the WindEEE Dome, at Western University in Canada. All wind speed raw signals that were recorded during the campaign are made publicly available in the Zenodo repository ([Canepa et al., 2024](#)). Particularly, this study will demonstrate that z_0 can change considerably the radial and vertical profiles of the mean wind speed and turbulence intensity, partly in analogy to what is observed in ABL winds.

The literature on this topic is still very limited. [Xu and Hangan \(2008\)](#) and [Mason et al. \(2009\)](#) conducted experimental investigations at small geometric scales, along with their numerical counterparts, focusing on the influence of the surface roughness on the developing wind speed profiles. The Reynolds numbers, Re , involved in their experimentation were 7.0×10^4 ([Mason et al., 2009](#)) and in the range 2.7×10^4 – 1.9×10^5 ([Xu and Hangan, 2008](#)). Their analogous findings demonstrated that an increase in z_0 decreases the maximum slowly varying mean wind speed \bar{V}_{\max} while increasing its height of occurrence z_{\max} . The offset of the two quantities with respect to the smooth surface case increases along the radial direction as turbulence developing in the near-wall region has more time to influence the flow field. The deviation from the smooth surface reference is expected to continue until a balance is reached between the wall friction and the flow shear in the outer layer. While [Xu and Hangan \(2008\)](#) found an offset starting near the jet touchdown position, [Mason et al. \(2009\)](#) observed a profile variation only for $r > r_{\max}$. However, the authors expected

noticeable variation in the profiles of \bar{V}_{\max} and z_{\max} along the entire measurement domain for higher Re , also supported by the results of [Xu and Hangan \(2008\)](#). We will verify these findings through the high Re values of present experiments which, to the authors' knowledge, are the highest explored in impinging jet (IJ) downburst-like physical investigations thus far. [Xu and Hangan \(2008\)](#) observed that $Re > 1.0 \times 10^6$ is required to meet the criterion $h_s^+ > 60$ and consider the flow in the “fully turbulent” regime ([White, 1991](#)). Here, $h_s^+ = u^* \cdot h_s / \nu$ is the dimensionless roughness parameter and depends on the average size of roughness elements, h_s , kinematic viscosity of the fluid, ν , and wall friction velocity, u^* . In this flow regime, the surface roughness governs the boundary layer formation, showing significant differences compared to the smooth surface with respect to the laminar flow regime at low Re .

The influence of various exposure conditions on downburst flows was further explored through numerical analysis employing large eddy simulations (LES). In this approach, surface roughness is implicitly modeled using fractal surfaces generated by random Fourier modes (RFM) ([Aboshosha et al., 2015](#)) and constant first grid point drag coefficients corresponding to the target roughness length ([Vermeire et al., 2011](#)). The selected methodology for simulating ground roughness exerts a significant influence on the outcomes of these latter studies, wherein the primary focus was to examine and enhance the overall numerical modeling of downburst winds. Due to the purely numerical nature of these investigations, we opt not to engage in a close comparison with our study here, as such a comparison might potentially introduce biased interpretations of the results. It is worth mentioning that analogous numerical investigations have also been employed recently with application to tornado-like vortices ([Gairola et al., 2023](#)).

The paper follows describing the experimental setup at the WindEEE Dome and the assessment of an equivalent full-scale roughness length for the tested surfaces (Sec. II). This is essential to fit the reduced-scale results into the full-scale scenario and potentially allows comparison analyses with downburst records in nature, following what mentioned above. Section III illustrates the methodology employed for decomposing and analyzing the wind speed records, providing a list of investigated parameters and considerations into the approach taken to address multiple experimental repetitions. Section IV presents the results, including a detailed physical description of the phenomenon, as well as the variations in the profiles of maximum velocity and its corresponding height, along with a comprehensive discussion on the flow turbulent characteristics, as dependent on Re and z_0 . Section V provides conclusions and insight for future developments of this research.

II. EXPERIMENTAL SETUP

The experiments were performed at the WindEEE Dome at Western University, Canada. WindEEE Dome is the first three-dimensional wind chamber capable of reproducing extreme wind events, with focus on tornadic and downburst winds ([Hangan, 2014](#)), at large geometric scales up to 1:100 ([Junayed et al., 2019](#) and [Romanic et al., 2020](#)). Technical details on the different operational modes of the laboratory, which can successfully run also ABL and shear flows, are reported by [Hangan et al. \(2017\)](#). In short, WindEEE Dome is comprised of an internal hexagonal chamber of equivalent diameter 25 m, surrounded by a 40 m diameter return circuit. The inner chamber has 100 fans, of which 60 are located on one of the six peripheral walls and are used to reproduce several types of ABL flows.

The remaining 40 fans are displaced in groups of eight at the bottom of the remaining five side walls and are mainly used to create tornado-like winds other than providing an outer section to the flow developed in the testing chamber [Fig. 1(a)]. An upper plenum hosts six larger fans (diameter of 2 m) that generate downburst and tornado flows in conjunction with the inner testing chamber. The two chambers are connected through an opening-closing nozzle system, or bell-mouth, comprised of mechanical louvers.

All of the raw experimental records presented and subsequently analyzed herein are accessible to the public in the Zenodo repository (Canepa *et al.*, 2024) under Creative Commons Attribution 4.0 International license, allowing users to conduct additional analyses.

A. Downburst generation inside the chamber

Downburst-like flows (DLFs) at the WindEEE Dome laboratory are produced by activating the six upper fans while maintaining the bell-mouth louvers closed to obstruct the flow passage to the testing chamber. When the desired pressure is achieved, roughly 3.4 hPa above atmospheric pressure in the upper plenum, the bell-mouth louvers abruptly open generating a dynamic downward impinging-jet flow inside the testing chamber. The bell-mouth louvers are closed 4 s later to create a transient downburst-like flow field. The nozzle diameter was set to $D = 3.2$ m, while $H = 3.8$ m was the nozzle-to-surface distance that leads to satisfy the condition $H/D > 1$ for which the downburst outflow and the associated PV fully develops, analogously to full-scale occurrences (Junayed *et al.*, 2019). Two jet intensities were used, corresponding to centerline jet velocities at the nozzle outlet section of $W_{jet} = 8.9$ and 12.4 m s^{-1} . The resulting jet Reynolds numbers were $Re = W_{jet}D/\nu = 1.92 \times 10^6$ and 2.68×10^6 ($\nu = 1.48 \times 10^{-5} \text{ m}^2 \text{ s}^{-1}$ is the kinematic viscosity of the air), which categorize the flow within the fully turbulent regime, according to the considerations outlined in the Introduction section, analogous to real downburst

conditions. The reduction of vertical pressure due to the horizontal constrain (i.e., the ground) causes the flow to propagate horizontally with radial symmetry and high intensity at the near-ground level. Upon exiting the peripheral fans, the flow recirculates upward through the upper fans and returns into the testing chamber [Fig. 1(b)], forming a closed-loop circuit.

B. Velocity measurements

Flow field was measured by means of 11 Cobra probes (manufactured by Turbulent Flow Instrumentation Pty Ltd) mounted on a stiff vertical mast to prevent vibrations in the flow. The measurement heights were $z = 0.040, 0.070, 0.100, 0.125, 0.150, 0.200, 0.300, 0.400, 0.500, 0.700,$ and 1.000 m AGL , which are hereafter presented in normalized form $z/D = 0.0125, 0.0219, 0.0313, 0.0391, 0.0469, 0.0625, 0.0937, 0.1250, 0.1563, 0.2187,$ and 0.3125 (rounded to the second decimal place in the following). The mast was moved to 10 subsequent radial locations ranging from $r = 0.64$ to 6.40 m , where r is the radial distance from the jet touchdown, with incremental steps of $\Delta r = 0.64 \text{ m}$. This corresponds to a range of normalized positions $r/D = 0.2\text{--}2.0$ with incremental steps $\Delta r/D = 0.2$ [Fig. 1(c)]. To avoid measurement distortions caused by irregularities of the chamber floor at $r/D = 0.8$, this particular measurement location was actually shifted to $r/D = 0.75$. The assumption of radial symmetry of the flow enabled to take measurements along a single azimuthal line [Fig. 1(a)]. Table I reports the measurements positions, along with the geometric and inflow kinematic setup parameters. For each r/D location, each experiment with the same inflow condition (i.e., jet velocity and diameter, rough surface) was repeated 10 times to have information concerning the variability of the results. A synchronization system at the bell-mouth level enabled the recording of the louvers opening and closing time. Based on this time, all experimental repetitions and velocity signals across the chamber were synchronized to statistically investigate the downburst outflow.

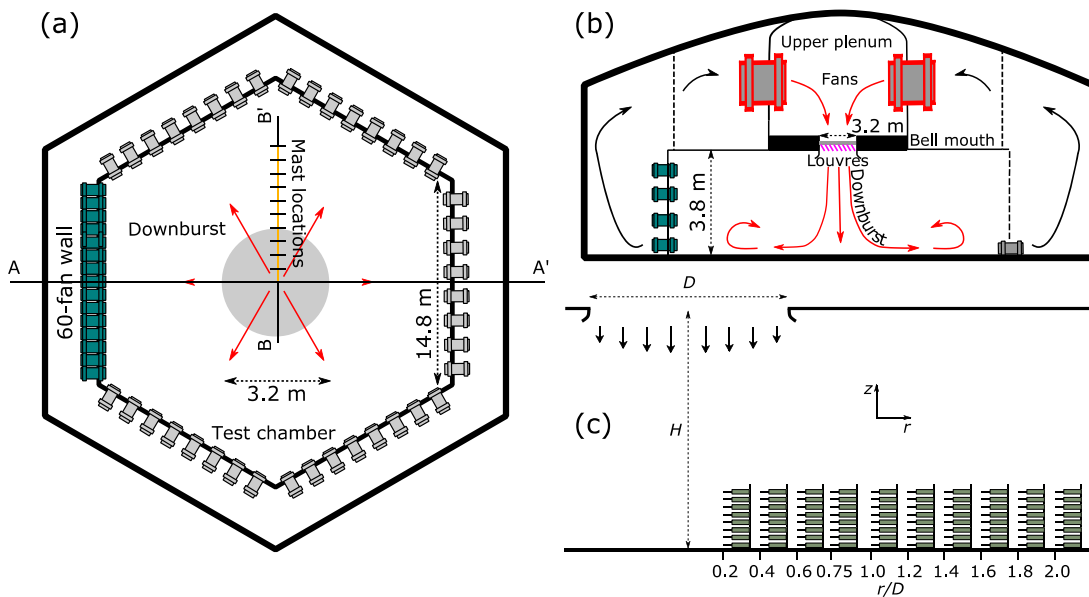


FIG. 1. Schematics of downburst flow generation and experimental setup: horizontal view (a) and vertical view at sections A-A' (b) and B-B' (c) [see (a)].

TABLE I. Geometric and kinematic experimental setup: case name; jet diameter (D); jet velocity (W_{jet}); jet Reynolds number (Re); equivalent roughness length ($z_{0,\text{eq}}$); normalized radial measurement locations (r/D); normalized measurement heights (z/D).

Case name	D (m)	W_{jet} (m s^{-1})	$\text{Re} \times 10^6$	$z_{0,\text{eq}}$ (m)	r/D	z/D
DB8.9-007	3.2	8.9	1.92	0.007	0.2–2.0 ^a	0.01, 0.02, 0.03, 0.04, 0.05, 0.06, 0.09, 0.12, 0.16, 0.22, 0.31
DB8.9-020	3.2	8.9	1.92	0.020	0.2–2.0 ^a	0.01, 0.02, 0.03, 0.04, 0.05, 0.06, 0.09, 0.12, 0.16, 0.22, 0.31
DB8.9-320	3.2	8.9	1.92	0.320	0.2–2.0 ^a	0.01, 0.02, 0.03, 0.04, 0.05, 0.06, 0.09, 0.12, 0.16, 0.22, 0.31
DB12.4-007	3.2	12.4	2.68	0.007	0.2–2.0 ^a	0.01, 0.02, 0.03, 0.04, 0.05, 0.06, 0.09, 0.12, 0.16, 0.22, 0.31
DB12.4-020	3.2	12.4	2.68	0.020	0.2–2.0 ^a	0.01, 0.02, 0.03, 0.04, 0.05, 0.06, 0.09, 0.12, 0.16, 0.22, 0.31
DB12.4-320	3.2	12.4	2.68	0.320	0.2–2.0 ^a	0.01, 0.02, 0.03, 0.04, 0.05, 0.06, 0.09, 0.12, 0.16, 0.22, 0.31

^aThe radial increment was $\Delta r/D = 0.2$. $r/D = 0.8$ was moved to $r/D = 0.75$ due to irregularities of chamber floor.

Cobra probes are multi-hole pressure devices designed to resolve the three velocity components in real time. They are conventionally named (U , V , and W) for the component along, transversal, and vertical to the probe axis, respectively. U is, here also, the radial outflow component of the downburst, since all Cobra probes faced the geometric position of jet touchdown, corresponding to $r/D = 0$. The probes provide reliable velocity measurements within a cone of $\pm 45^\circ$ in respect to the instrument horizontal axis. The reported accuracy of Cobra probes from the manufacturer is $\pm 0.5 \text{ m s}^{-1}$ and $\pm 1^\circ$ for velocity and yaw/pitch angles, respectively, up to approximately 30% of turbulence intensity. The sampling frequency of all velocity measurements was $f_s = 2500 \text{ Hz}$. All velocity measurements below 1 m s^{-1} were removed from the analysis due to the poor accuracy of Cobra probes below this threshold.

C. Rough surfaces

Three different surfaces were deployed for roughness testing: (i) WindEEE bare floor; (ii) carpet; and (iii) artificial grass [Figs. 2(a)–2(c)]. The selected surfaces had sizes of $1 \times 8 \text{ m}^2$ (width \times length) and were displaced along the azimuth line of measurement with a 1 m offset with respect to the geometric position of jet centerline, covering a longitudinal extent up to about $r/D = 2.2$. Each surface was characterized with an equivalent full-scale roughness length $z_{0,\text{eq}}$ determined through simulations of only ABL-like conditions within the testing chamber. This includes the WindEEE bare floor which is not a perfect smooth surface due to irregularities across the surface. A total of 15 different ABL-like profiles were tested inside the chamber by varying the rotation-per-minute (rpm) of the fans across the four rows of the 60-fan wall. A specific setup of the four fan rows (50%–70%–60%–50% rpm of the fans' nominal power, from floor) and a length scale of $\Lambda_l = 1:200$ were chosen based on correlation between physically reproduced ABL wind speed profiles and curve fitting through Eq. (A1.8) of the ESDU (Engineering Science Data Unit) 82026 (2002) [Figs. 2(d)–2(f)]. This scale also proves to be reasonable for both downburst and ABL flows at the WindEEE Dome (Romanic *et al.*, 2020). According to this scale, the resulting full-scale equivalent measurement heights z_{eq} range from 8 to 200 m which also approximately covers the vertical measurement extent of a LiDAR Wind Profiler (Canepa *et al.*, 2020). The full-scale equivalent downdraft diameter $D_{\text{eq}} = 640 \text{ m}$ may be associated with a microburst (Fujita, 1985 and Hjelmfelt, 1988). A full-scale equivalent roughness length was determined for the three tested surfaces by linearly fitting the measured data on the chart $U - \ln(z)$

using the logarithmic law-of-the-wall depending on two parameters, namely, friction velocity u_* and roughness length z_0 . From here, $z_{0,\text{eq}} = 0.007, 0.02$, and 0.32 m are calculated according to the value of Λ_l . These values, respectively, correspond to (i) smooth surface with negligible vegetation and obstacles (e.g., beaches, snow-covered open area, farmland); (ii) cultivated area with regular cover of medium crops, occasional to scattered obstacles (e.g., shelterbelts, vineyards); and (iii) rough surface with recently developed high crops and rather large obstacles (farms, forest, suburban) (ESDU 82026, 2002). While traditional boundary layer wind tunnels (BLWTs) naturally produce an ABL-like profile along the chamber length using active and passive control devices (e.g., grid, roughness elements, and spires), WindEEE Dome mechanically generates an ABL-like profile by adjusting the fan rpm at the 60-fan wall. This results in vertical profiles of turbulent intensity that deviate from the ESDU standards (not shown here). However, in the context of downburst winds, Romanic and Hangan (2020) observed that the turbulence intensity profiles generated inside the isothermal chamber of the WindEEE Dome resemble to a good extend the unstable atmospheric conditions prior to thunderstorm events.

All results presented hereafter will be referred to the equivalent $z_{0,\text{eq}}$ defined above for the purpose of comparison and applicability to full-scale measurements. These values correspond to real down-scaled $z_{0,\text{real}} = 3.5 \times 10^{-5}$, 1.0×10^{-4} , and $1.6 \times 10^{-3} \text{ m}$, respectively. Comparisons with previous literature studies will also require a conversion factor to match our z_0 values with different equivalent sand-grain roughness heights Δ (Xu and Hangan, 2008 and Mason *et al.*, 2009). Several experimental and numerical approaches have introduced simplified formulations to derive z_0 based on the geometric characteristics of roughness elements, specifically the average three-dimensional (3D) dimensions of obstacles and their spacing (e.g., Lettau, 1969; Stearns, 1970; and De Bruin and Moore, 1985). Considering the nature of the rough surfaces used in our investigation (carpet, artificial grass) and in prior studies (sandpaper), along with the inherent difficulty in determining the average 3D dimensions of the elements, we have chosen to employ the empirical relationship from Davenport (1963), $z_0 = \Delta/30$. In doing so, we aim to qualitatively compare disparate experimental approaches and scaling. Therefore, the resulting equivalent heights of the rough surfaces utilized in the present study are $\Delta = 0.001, 0.003$, and 0.048 m , which yield normalized values $\Delta/D = 0.00031, 0.00094$, and 0.0150 , respectively, for WindEEE bare floor, carpet, and artificial grass surfaces.

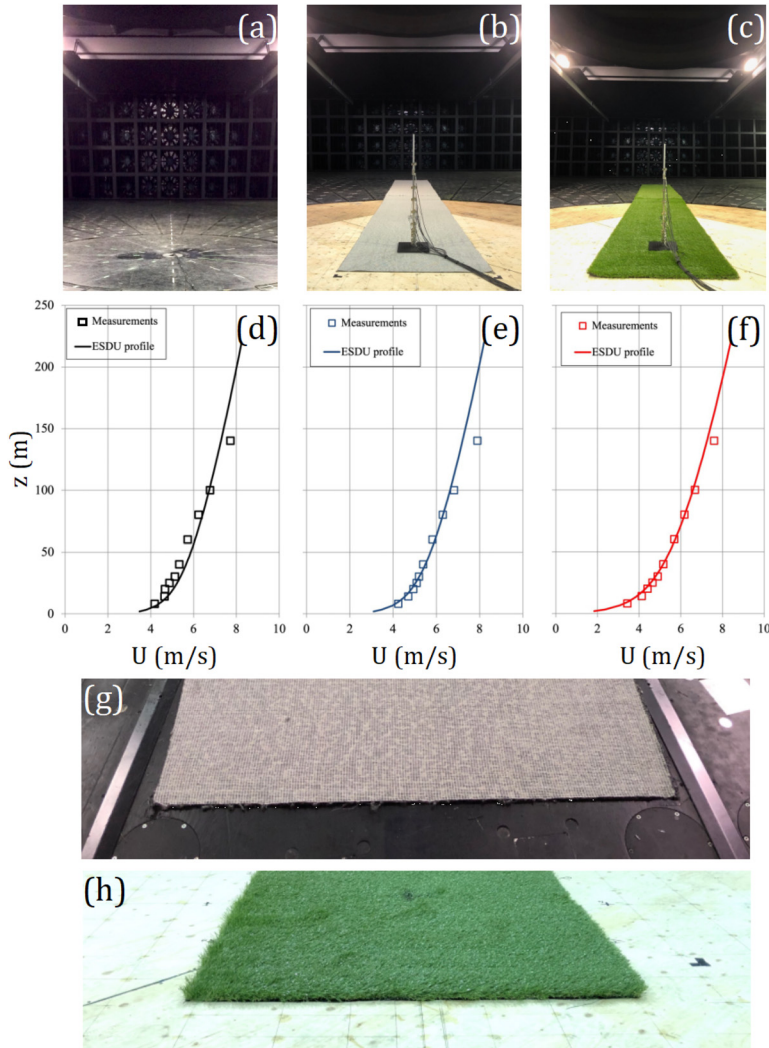


FIG. 2. Rough surfaces: WindEEE bare floor (a) and (d); carpet (b), (e), and (g); artificial grass (c), (f), and (h). Setup photographs (a)–(c) and comparison between wind speed measurements (at the central point of the chamber) and Eq. (A1.8) of ESDU 82026 (2002) (d)–(f); zoom-in of carpet (g) and artificial grass (h) surfaces.

III. METHODOLOGY

The wind speed signals were analyzed in terms of slowly varying mean wind speed, $\bar{V}(t)$, and turbulence intensity modulated on $\bar{V}(t)$. They are evaluated through the classic downburst decomposition technique (Solari *et al.*, 2015) where the resultant horizontal wind speed $V(t)$ is decomposed into

$$V(t) = \bar{V}(t) + V'(t). \tag{1}$$

The residual turbulent fluctuation $V'(t)$ can, in turn, be expressed as the product of its slowly varying standard deviation $\sigma_V(t)$ by a reduced turbulent fluctuation $\bar{V}'(t)$ dealt with a stationary Gaussian random process with zero mean and unit standard deviation. The slowly varying turbulence intensity is thus evaluated through

$$I_V(t) = \sigma_V(t)/\bar{V}(t). \tag{2}$$

All quantities introduced are determined through a moving-average filter with mobile time window $\Delta t = 0.1$ s. This value was derived

through a parametric investigation applied to WindEEE Dome wind speed signals by Junayed *et al.* (2019). The findings indicated that a 0.1 s mobile window is optimal for effectively distinguishing the large-scale mean wind structure (at the low frequencies) from the small-scale turbulence fluctuations (at the high frequencies).

All results presented hereafter refer to parameters assessed individually for each experimental repetition and, only in the final stage, calculated as the ensemble average of the 10 repetition values.

The effect of roughness length on the low-frequency content of the flow will be assessed mainly in terms of variation of the maximum slowly varying mean wind speed and its corresponding occurrence position. Both parameters will be named according to their computation domain as reported in Table II.

For the sake of conciseness, Figs. 5–8 show the results only for $Re = 1.92 \times 10^6$. The lower jet intensity $W_{jet} = 8.9 \text{ m s}^{-1}$ reduces the transiency of the phenomenon compared to $W_{jet} = 12.4 \text{ m s}^{-1}$ for $Re = 2.68 \times 10^6$, thereby highlighting the hallmarks of the influence of ground roughness on the evolving flow.

TABLE II. Symbols' nomenclature for maximum wind speed and its occurrence position.

Parameter	Interpretation
$\bar{V}_{\max}(r)$	Maximum of \bar{V} across t and z , as a function of r
$\bar{V}_{\max}(z)$	Maximum of \bar{V} across t and r , as a function of z
$\bar{V}_{\max}(t)$	Maximum of \bar{V} across z , as a function of t
\hat{V}_{\max}	Overall maximum of \bar{V} (across t , r , and z) for a specific z_0 and Re
\hat{V}	Overall maximum of \bar{V} (across t , r , z , and z_0) for a specific Re
z_{\max}, r_{\max}	Measurement positions of occurrence of \bar{V}_{\max} in the different forms above
\hat{z}_{\max}	Height of occurrence of \hat{V}_{\max}

The results in Sec. IV are presented in terms of ensemble average across the 10 experimental repetitions. However, the deviation among experiments is graphically represented mostly by means of error bars, evaluated as standard error, $\sigma_E = 2\sigma/\sqrt{N}$, where σ is the measurement standard deviation among repetitions and N is the number of repetitions ($N = 10$). The variation across experiments is pronounced at the beginning and ending of the radial domain of measurements due to the high-flow mixing, and hence turbulence, in correspondence to the jet-impinging region and to the locations further away from the jet touchdown.

For comparison with full-scale downburst records, a normalized time $\tau = t \cdot f_v$ is introduced based on the shedding frequency of eddies from the bell mouth, f_v . Details on its formulation are reported in Canepa et al. (2023b). Adopting the empirical expression of Popiel and Trass (1991), we obtain a Strouhal number $St = 0.72$, which leads to vortex shedding frequencies $f_v = St \cdot W_{jet}/D = 2.00$ and 2.79 Hz, respectively, for $Re = 1.92 \times 10^6$ and 2.68×10^6 . It follows that 8 to 10 vortices shed during the nozzle opening $\Delta t = 4$ s, which are substantially more than the average 2.5 vortices expected in a 10 min full-scale downburst event (Canepa et al., 2023b).

IV. RESULTS

A. Physical characterization of the phenomenon

Canepa et al. (2022c) defined three stages of the downburst wind speed signal: (1) PV, (2) plateau, and (3) dissipation segments [Fig. 3(a)]. They, respectively, correspond to: (1) recording of the PV passage over the measuring instrument, which is marked by a sudden ramp-up of the wind speed, followed by its peak and consequent ramp-down; (2) subsequent weaker trailing vortices produce a randomly fluctuating flow with a mean value fairly constant over time; (3) downdraft dissipation or moving away from the instrument. Full-scale records may not show a plateau segment for early-dissipating or rapidly moving downdraft. This scenario could also arise in instances of short horizontal extensions of the outflow, such as in the case of microbursts [where the outflow's size is smaller than 4 km, as defined by Fujita (1985)]. A notable illustration is the well-known Andrews AFB microburst (Fujita, 1983).

Figure 4 depicts a vertical view of the evolving flow field captured at five different time instants. The downdraft stage of the phenomenon shows invariant kinematic and geometric characteristics among the z_0 cases and reproduced times. The flow is directed downward at the higher heights and radially up to $r/D = 0.8$. In this radial range, streamlines change their orientation from vertical to horizontal by approaching the ground. The PV lands on the surface at this approximate radial location and produces the maximum outflow intensity while transiting over $r/D = 1.0$ at $\tau = 4.40$ [Figs. 4(a)–4(c)]. Here, surface roughness has substantial impact on the developing outflow in terms of height of both the PV core and the corresponding region of maximum flow intensities at its lower boundary (brighter contour colors in Fig. 4). Commencing at $\tau = 4.72$, the PV core elevates above the ground as a result of the boundary layer separating from the surface. This phenomenon arises from the interaction between PV and a secondary recirculation bubble known as the secondary vortex (SV), formed at the outflow front due to the air being expelled outward by the expanding PV (Canepa et al., 2022b). White dashed contours in Fig. 4(f) schematizes this dynamics. The same schematics is not applied to the other subfigures of Fig. 4 due to the qualitative and not-to-scale characteristics of this representation. However, Junayed et al. (2019) estimated through

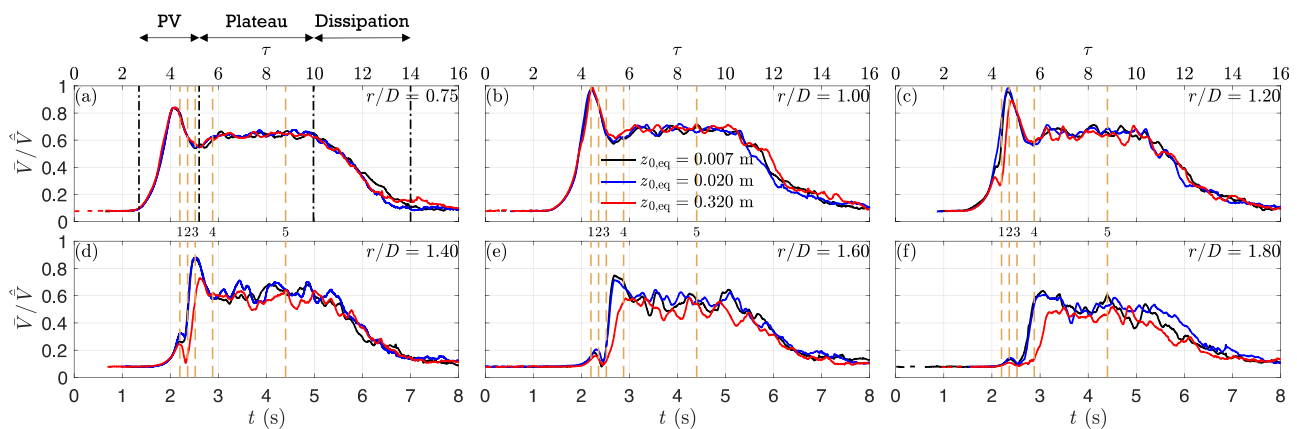


FIG. 3. 10-repetition ensemble mean of slowly varying mean wind speed for $Re = 1.92 \times 10^6$. Orange dashed lines define time stamps reproduced in Fig. 4.

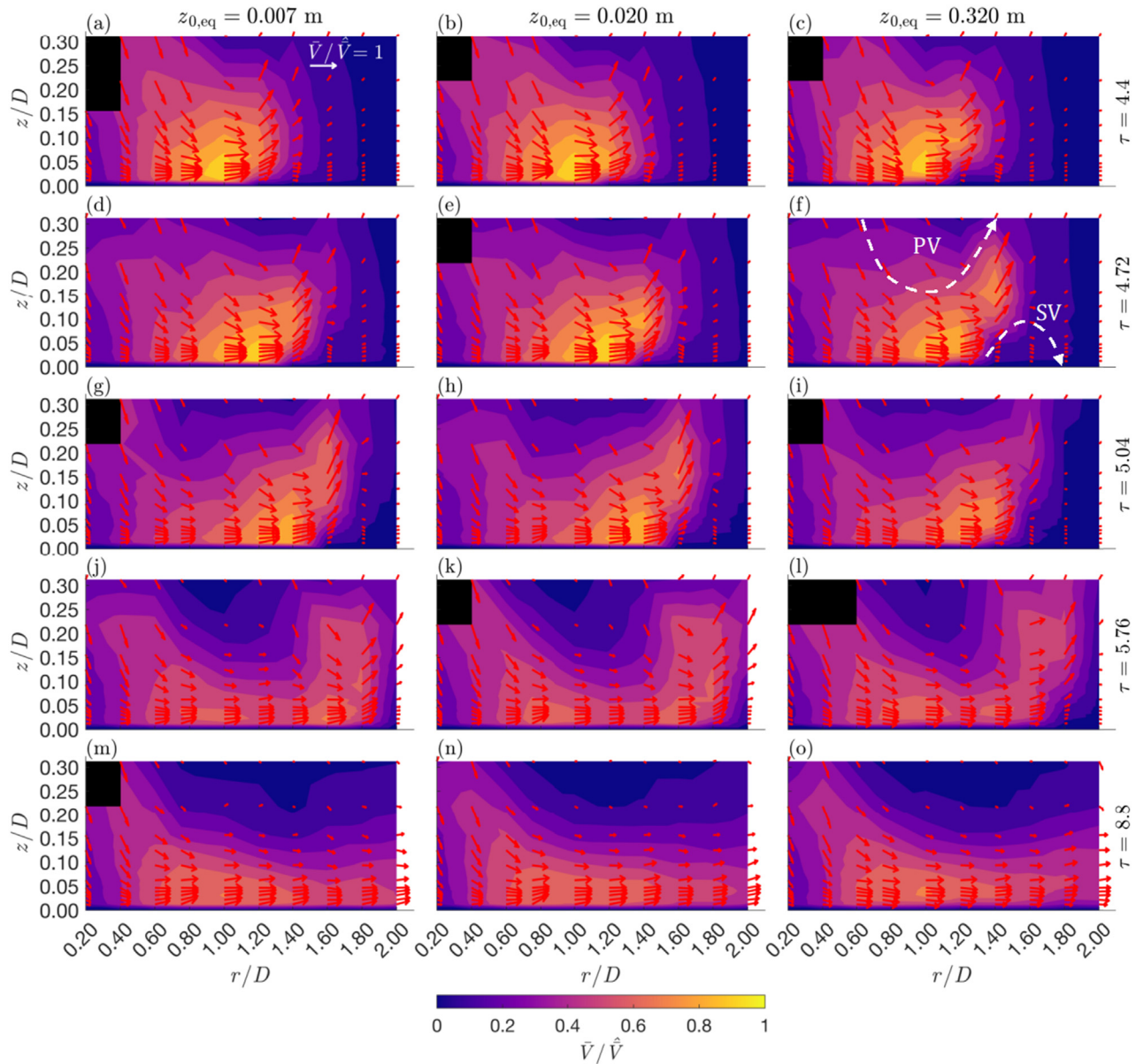


FIG. 4. Flow field (vertical view) for the three z_0 cases (columns) and time stamps (rows) depicted in Fig. 3 (see vertical orange dashed lines). Black spots identify regions where wind speed is below 1 m s^{-1} (disregarded due to accuracy of Cobra probes). Red vectors represent the actual point Cobra probes' measurements, while contour maps are obtained from their interpolation. Note that the orientation of Cobra probes' head toward the jet impingement makes unfeasible to measure the backward flow produced by PV and SV circulations.

Particle Image Velocimetry (PIV) methods a height and vertical extension of the PV core of approximately $z/D = 0.22$ and 0.16 , respectively, for bare-floor impinging surface and analogous Re . In our experiments, surface roughness clearly enhances the surface layer separation. Despite the wind speed maxima are still observed underneath the PV structure, a second region of high flow intensities develops at the PV-SV interface at higher heights and ahead of PV. Here, the opposite circulations of PV and SV [see Fig. 4(f)] channels the flow upward. The

height of this interaction does not change among the z_0 cases. However, the boundary layer separation and interaction with outer layer, respectively, corresponding to SV and PV circulation zones, onsets at different times and radial distances: first at $\tau = 4.72$ and $r/D = 1.2-1.4$ for $z_{0,eq} = 0.320 \text{ m}$; later at $\tau = 5.04$ and $r/D = 1.6$ for the lower z_0 cases, $z_{0,eq} = 0.007$ and 0.020 m . At this moment, the PV-SV interaction already fades for $z_{0,eq} = 0.320 \text{ m}$, as suggested by the magnitude of wind speed vectors ahead of PV. This is due to

the stronger PV vorticity that uplifts the SV and eventually ejects it from the PV surface. Going forward in time, at $\tau = 5.76$, a third high-intensity bubble pops out behind the PV. This is the signature of the first trailing vortex produced after PV. The boundary layer reattaches to the surface and streamlines are again directed longitudinally (see $\tau = 8.80$ in Fig. 4).

B. Variation of wind speed profiles with z_0

In their papers, Xu and Hangan (2008) and Mason et al. (2009) discussed the role that surface roughness plays on the radial and vertical profiles of the horizontal wind speed. They focused particularly on the maximum velocity magnitude and its height of occurrence, \bar{V}_{max} and z_{max} , respectively. Figures 5–7 confirm the past findings: an increase in the roughness length z_0 reduces the maximum velocity \bar{V}_{max} and raises its height above the ground z_{max} . $z_{0,eq} = 0.320$ m clearly enhances this concept. Analogously to Mason et al., the offset of \bar{V}_{max} commences in the vicinity of the location of overall maximum wind speed in the flow field, i.e., $r/D = 1.0$ [Figs. 5(a), 6(a), and 7(c)–7(h)]. At this location, the boundary layer that develops beneath the evolving PV following the jet touchdown begins to detach. The deviation of the three roughness cases possibly last beyond the boundary of the measurement domain. A re-equilibrium in this sense would occur where and when the wall friction in the inner layer and the flow shear in the outer layer balance again each other. Conversely, Xu and Hangan (2008) noted a deviation of \bar{V}_{max} and z_{max} with respect to z_0 beginning closer to the jet touchdown at the ground. Mason et al. (2009) speculated that the discrepancy between the two studies stemmed from the lower Re adopted in their study compared to that of Xu and Hangan. However, our large-Re ($Re > 1.0 \times 10^6$) experiments lead to a reduction in \bar{V}_{max} only for $r > 1.0 D$ [Fig. 5(a)], while causing variations in its height z_{max} across the entire radial domain [Fig. 6(a)]. As expected, z_{max} increases with z_0 beyond the location of absolute maximum wind speed ($r/D = 1.0$). However, in the stagnation downdraft-like region (i.e., $r/D < 1.0$), z_{max} decreases with increasing z_0 [Fig. 6(a)], except at $r/D = 0.2$ where flow is mainly directed downward. This might occur because rougher surfaces retain the impinging flow and PV closer to the ground. Interestingly, at $r/D = 2.0$ and for $z_{0,eq} = 0.320$ m, z_{max} decreases to similar values with respect to the two lower z_0 cases.

Examining Figs. 5(a) and 6(a), \hat{V}_{max} aligns with the minimum of z_{max} at $z_{0,eq} = 0.007$ and 0.020 m, while it occurs at higher elevations near $z/D = 0.04$ for $z_{0,eq} = 0.320$ m. Figure 7 shows vertical profiles with consistent patterns above z_{max} for $r/D \leq 1.2$, while deviations become noticeable beyond this point. Here, the top measurement height records a larger velocity for $z_{0,eq} = 0.320$ m compared to the two lower- z_0 cases. The surface layer separation, indicated by an increase in z_{max} beyond $r/D = 1.0$ with increasing z_0 , is clearly depicted in Fig. 7. In fact, the PV–SV interaction produces an increase in the boundary layer thickness and thus of z_{max} . The subsequent decrease in z_{max} is due to the ejection of SV from the PV surface and reduction of boundary layer thickness. This confirms the role of roughness-related turbulence to influence the outflow boundary layer which, in turn, affects the outer layer above z_{max} .

Figure 8 substantiates the influence of surface roughness on altering the geometric and kinematic properties of the downburst outflow. In terms of maximum velocity, a deviation of $z_{0,eq} = 0.320$ m from the two lower-roughness cases is observed starting from $r/D = 1.2$: this also includes an increasing time shift related to the passage of the PV (i.e., the absolute maximum) along the radial domain of measurements, particularly at further locations from the jet touchdown [see dashed lines in Figs. 8(a)–8(f)]. This suggests that the downburst outflow and the leading PV are slowed down by surface roughness while expanding laterally. Before the onset of the downburst outflow z_{max} , that is here assumed as a time-dependent variable $z_{max} = z[\bar{V}_{max}(t)]$, sets to higher values partly due to the vertical IJ flow (i.e., downdraft flow in nature) that is stronger at the higher heights while deflecting horizontally due to the constrain at the ground, and partly to the interaction between viscous and inviscid regions (i.e., inner and outer surface layers) (Canepa et al., 2022b). With the passage of the PV, the outflow is constrained underneath the vortex itself and z_{max} drastically decreases to the lower heights (Canepa et al., 2022b). In other terms, Figs. 8(g)–8(l) shows the development of the surface layer as dependent from z_0 . Precisely, for locations close to the impingement zone (approximately $r/D < 1.2$), the passage of the PV produces a boundary layer that remains confined between the vortex lower end and the ground. Beginning at $r/D = 1.2$, a separation of the surface layer from the ground is observed. The extent of this separation increases with z_0 , emphasizing a strong influence on the turbulence generated by the

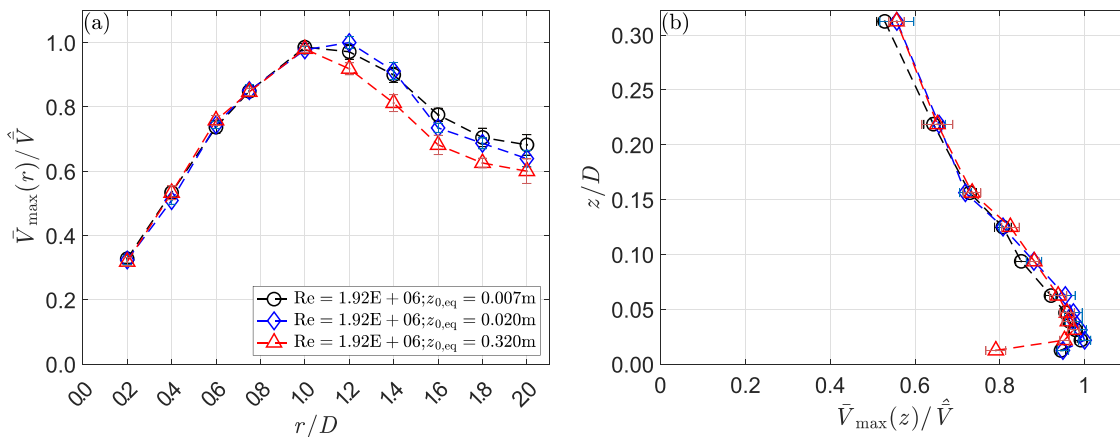


FIG. 5. Variation in maximum velocity \bar{V}_{max} as a function of radial r (a) and height z (b) measurement positions for $Re = 1.92 \times 10^6$.

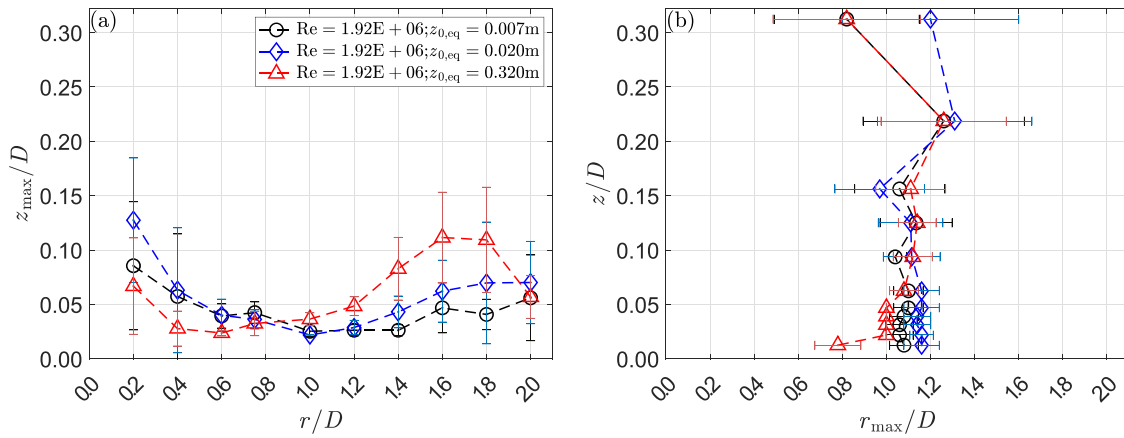


FIG. 6. Height of maximum velocity z_{\max} as a function of radial r position (a) and radial position of maximum velocity r_{\max} as a function of height z (b) for $Re = 1.92 \times 10^6$.

surface roughness. The flow separation–reattachment, which leads to the formation of the SV, is reflected in the signals through an increase in z_{\max} [see dashed lines in Figs. 8(i)–8(l)] during the ramp-up stage of the wind speed, right before the peak that marks the passage of the PV. The dashed lines in Figs. 8(i)–8(l) highlight a temporal displacement of the z_{\max} peaks along the radial distance. This shift occurs due to boundary layer separation, resulting in PV and flow deceleration. The expanding size of SV with z_0 is thus accountable for increasing outflow decelerations at larger radial positions. At $r/D = 1.8$, the SV is likely being ejected from the PV surface for $z_{0,\text{eq}} = 0.320\text{m}$ and flow decelerations become more pronounced for the two lower-roughness cases. The plateau and dissipation segments of the signal are denoted by a very limited variability among the z_0 cases. These findings demonstrate that the influence of surface roughness is significant only for the maximum wind

speed and its corresponding height. It follows that the roughness length of the terrain is a fundamental parameter to adequately assess and model the maximum intensity stage of the downburst phenomenon.

The overall maxima of the wind speed \hat{V}_{\max} over the entire flow field do not show correlation with z_0 [Fig. 9(a)]. Only a slight decrease in \hat{V}_{\max} with increasing z_0 is found for $Re = 2.68 \times 10^6$. Interestingly, while $\hat{V}_{\max} \approx 1.5 \cdot W_{\text{jet}}$ for $Re = 1.92 \times 10^6$ in analogy to previous studies in the literature (Canepa et al., 2022b), $Re = 2.68 \times 10^6$ presents a $\hat{V}_{\max}/W_{\text{jet}}$ ratio that is larger than 1.6. Therefore, in our study, this ratio depends on Re . The height \hat{z}_{\max}/D presents a robust increase from 0.022 to 0.031 for the highest roughness-case $z_{0,\text{eq}} = 0.320\text{m}$, while the two lower- z_0 cases present same height of the overall maximum. Same \hat{z}_{\max}/D are obtained for both Re .

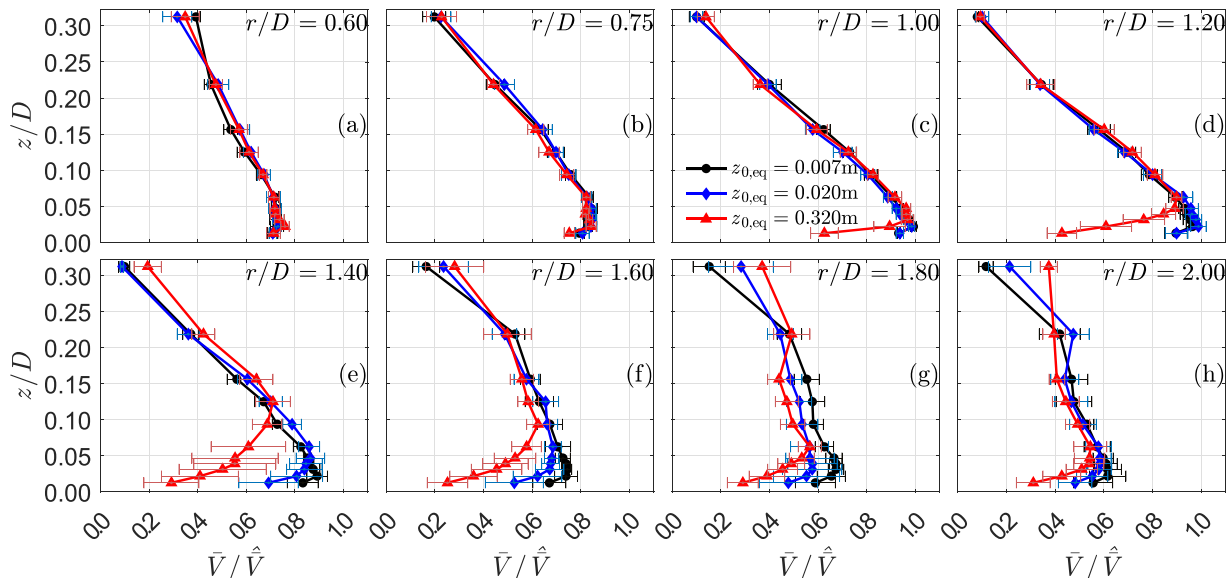


FIG. 7. Vertical profiles of \bar{V} (repetitions' ensemble and variation) at the time of $\bar{V}_{\max}(r)$ at $r/D = 0.6$ – 2.0 [(a)–(h)] for the three rough surfaces and $Re = 1.92 \times 10^6$.

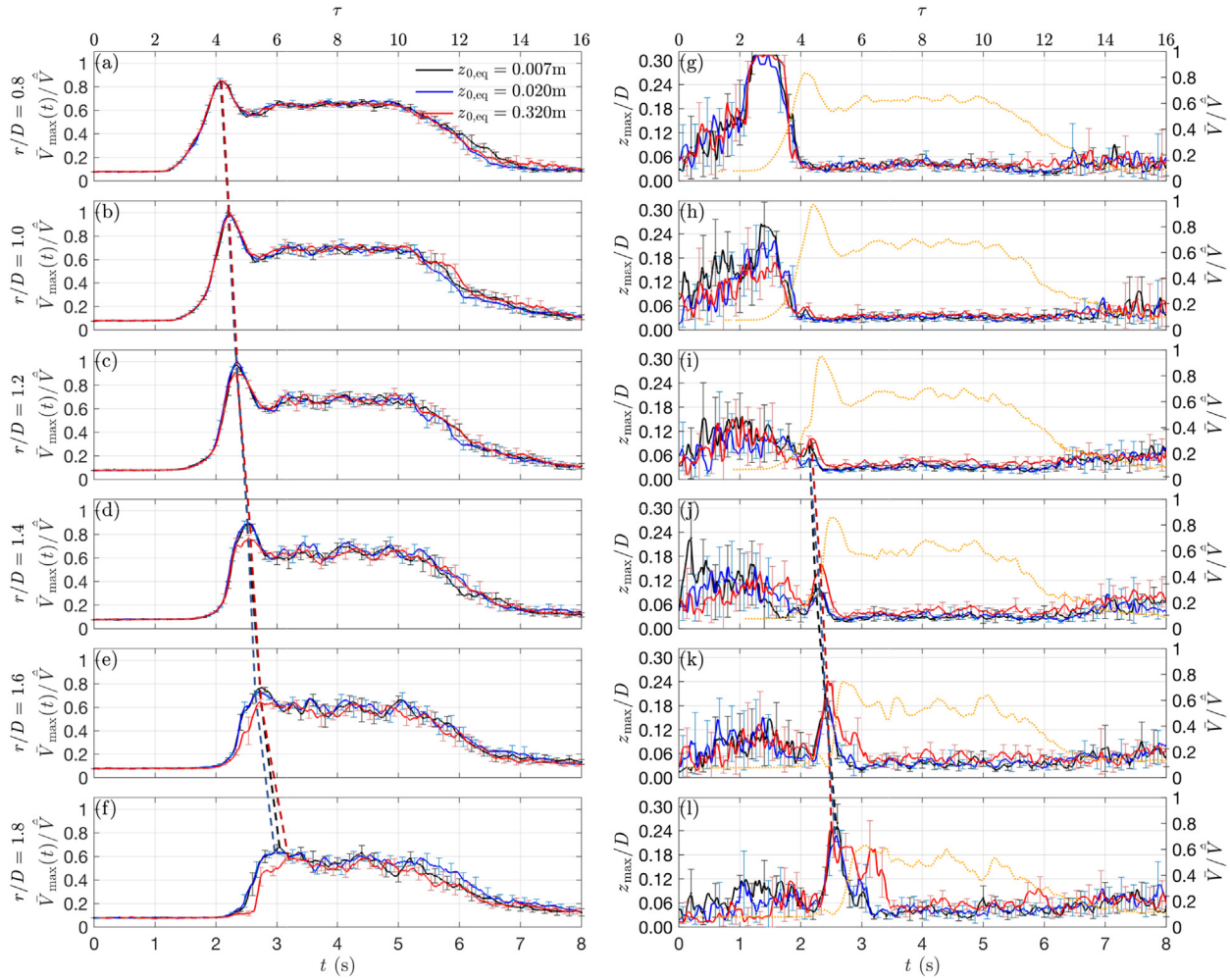


FIG. 8. Time series of maximum velocity \hat{V}_{\max} (a)–(f) and its height $z_{\max} = z[\hat{V}_{\max}(t)]$ (g)–(l) for $r/D = 0.8$ – 1.8 and $Re = 1.92 \times 10^6$. In graphs (a)–(f), dashed lines connect the maxima of \hat{V}_{\max} for the different z_0 cases. In graphs (g)–(l), dashed lines connect z_{\max} only across radial locations where surface layer separation is clear, i.e., $r/D > 1.0$. In graphs (g)–(l), orange lines represent the repetition-ensemble time series of the slowly varying mean wind speed for $z_{0,eq} = 0.007\text{ m}$ at the specific radial location and $z/D = 0.03$.

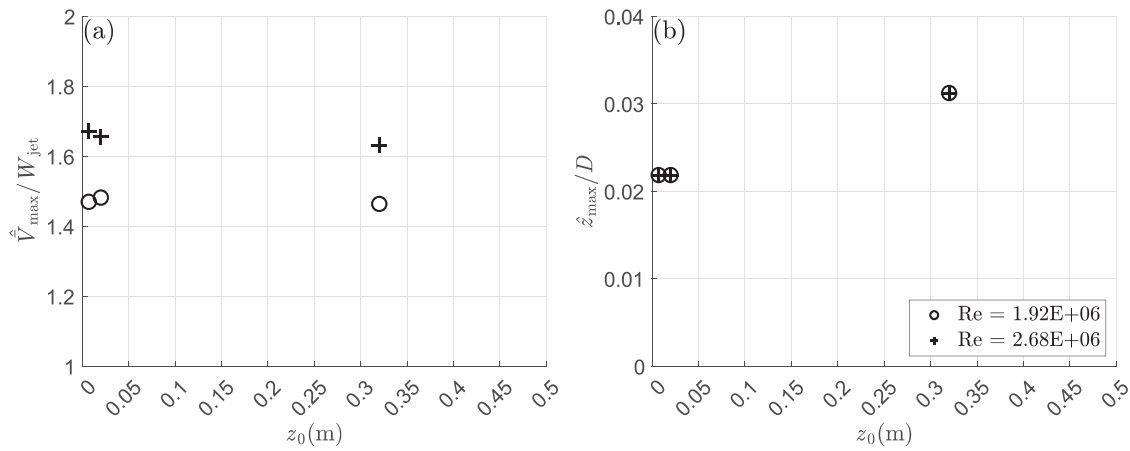


FIG. 9. Maximum wind speed over the entire flow field \hat{V}_{\max} (a) and its height \hat{z}_{\max} (b) for the two Re cases as dependent on z_0 .

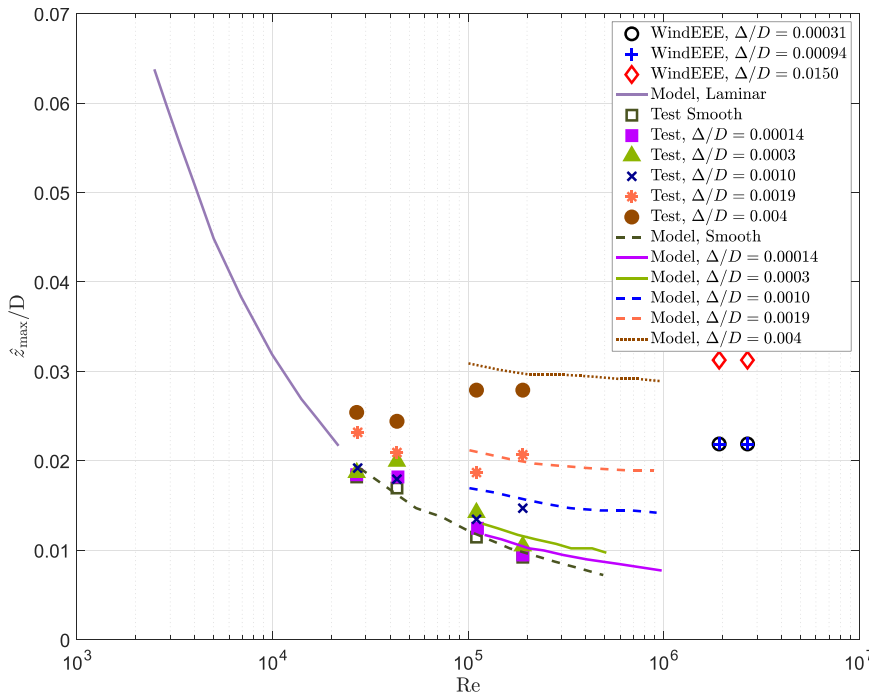


FIG. 10. Height of maximum wind speed \hat{z}_{max} as a function of Re and equivalent average height of roughness elements, Δ . Comparison with experimental (“Test”) and numerical (“Model”) results of Xu and Hangan (2008).

Figure 10 shows that the variation in \hat{z}_{max} with Δ does follow the general trend observed by Xu and Hangan (2008) at lower Re. However, comparing our cases $\Delta/D = 0.00031$ and 0.00094 with the experimental and numerical curves $\Delta/D = 0.0003$ and 0.0010 of Xu and Hangan (2008), we find higher \hat{z}_{max} values. This discrepancy is possibly caused by the surface layer separation and interaction between PV and SV, which may not occur at lower Re. The largest roughness height that was tested in our study, i.e., $\Delta/D = 0.0150$, is much higher than any roughness tested by Xu and Hangan.

C. Variation of turbulence profiles with z_0

Vertical profiles of turbulence intensity I_V , evaluated through Eq. (2), are significantly affected by surface roughness (Fig. 11). This mirrors the features of wind speed vertical profiles depicted in Fig. 7. Turbulence intensity varies greatly with z_0 at the lower heights and up to the height of maximum velocity z_{max} , where I_V reaches a minimum. Above z_{max} , profiles follow analogous pattern. Some differences are observed at $r/D = 2.0$ [Figs. 11(b), 11(d), 11(f), and 11(h)]. Here, I_V assumes larger values at the higher heights with respect to the location

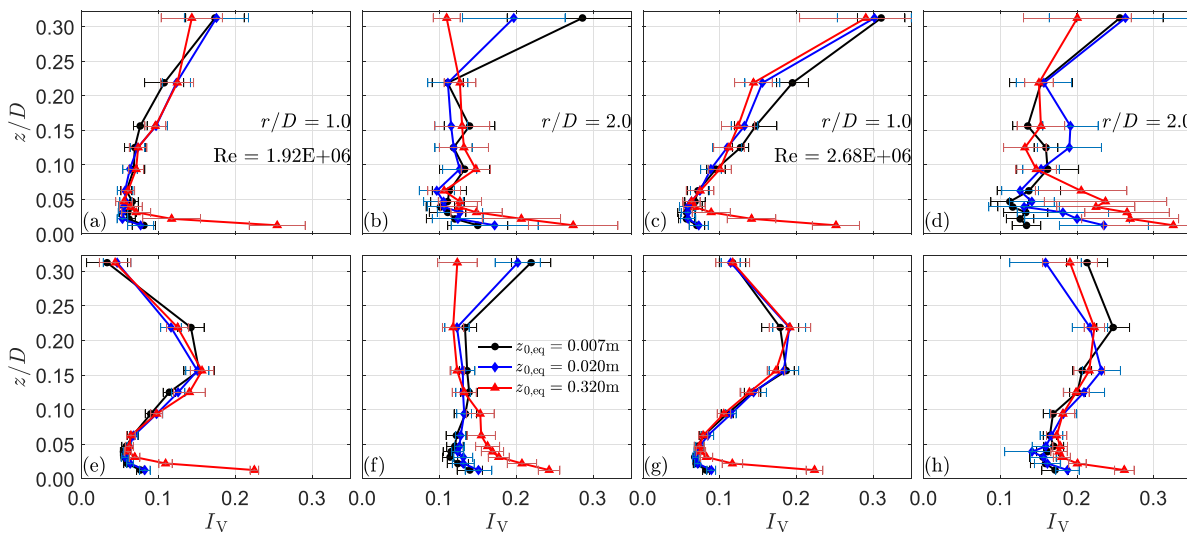


FIG. 11. I_V profiles during passage of PV (a)–(d) and plateau (e)–(h) segments of the wind speed signal, for $r/D = 1.0$ [(a), (c), (e), and (g)] and $r/D = 2.0$ [(b), (d), (f), and (h)], $Re = 1.92 \times 10^6$ [(a), (b), (e), and (f)] and $Re = 2.68 \times 10^6$ [(c), (d), (g), and (h)].

$r/D = 1.0$, at least during the PV segment [Figs. 11(a), 11(b), 11(e), and 11(f)]. This may be due to the structure of the developing outflow that gains turbulence by moving outward along the radial distance (Canepa *et al.*, 2022b). A further contribution to this is provided by the turbulence generated by the ground roughness.

I_V sets to large values in the range $I_V = 0.2$ – 0.3 for the highest-roughness case $z_{0,eq} = 0.320$ m and below z_{max} . This observation remains consistent across various radial positions and time intervals, clearly indicating that z_0 significantly amplifies the intensity of I_V at the near-ground level. This finding holds particular relevance for civil and wind engineering applications. These magnitudes double or more those related to the two lower-roughness cases ($z_{0,eq} = 0.007$ and 0.020 m) at $r/D = 1.0$ [Figs. 11(a), 11(c), 11(e), and 11(g)], while the ratio decreases slightly below 2 at $r/D = 2.0$ [Figs. 11(b), 11(d), 11(f), and 11(h)]. However, DLFs do not actually increase the maximum magnitudes of turbulence intensity at the near-ground level with respect to ABL-like flows (not shown here), where the turbulence level decreases quasi-monotonically with the height. The DLF profile's shape at $r/D = 2.0$ looks alike between PV [Figs. 11(b) and 11(d)] and plateau [Figs. 11(f) and 11(h)] segments of the wind speed signal. Nevertheless, substantial distinctions become apparent in close proximity to the jet impingement, where the profiles adopt a C-like shape at the PV segment [Figs. 11(a) and 11(c)] while a reversed-S-like shape is observed at the plateau segment of the velocity signal [Figs. 11(e) and 11(g)]. This latter resembles to a good extent the turbulence profile found by Xu and Hangan (2008) at $Re = 1.9 \times 10^5$ where, however, the I_V gradient along the height was enhanced with respect to our results at higher Re . Numerical investigations, as outlined by Aboshosha *et al.* (2015), yielded overall higher turbulence intensities (up to 40%) with respect to our values, with peaks occurring at the ground level and a decreasing trend along the height. Furthermore, these maxima are observed beyond the radial position $r/D = 1.5$ and ahead in the radial direction with respect to the wind speed peaks. Nevertheless, in their study, turbulence intensity was computed using a different calculation scheme that may also contribute to the noted discrepancies mentioned above.

The I_V increase at the top of the profiles is partly expected and is related to the PV passage [Figs. 11(a)–11(d)] that produces high wind speeds below its structure and a strong reduction by moving upward toward the inner vortex core (Canepa *et al.*, 2022b). This decrease in \bar{V} causes I_V to increase [Eq. (2)]. On the other hand, this enhances the significance of the large I_V values observed at the near-ground level. I_V does not increase at the top heights during the plateau segment of the signals where the PV has already moved away from the measuring instrument.

V. CONCLUSIONS AND PROSPECTS

This paper addresses the effects of surface roughness on experimentally produced downburst outflows. It is well established that the roughness term strongly shapes the governing equations and wind profiles of synoptic-scale extra-tropical cyclones in the atmospheric boundary layer (ABL). Thunderstorm downbursts are completely different phenomena, characterized by significant non-stationarities and localized behavior both in space and time. Furthermore, the wind vertical profile does not follow the characteristic logarithmic-like pattern typical of extra-tropical depressions, where the roughness length z_0 clearly affects the height and shape of the developed boundary layer. In fact, the wall jet-type flow developed upon the downdraft impingement

on the ground produces maximum horizontal velocities close to the surface which lead to a typical nose-shaped profile during the most intense stage of the storm. The present study assesses whether the parameter z_0 plays an important role also for the near-ground boundary layer produced at the downburst outflow. In fact, the rapid outflow dynamics may not enable the ground roughness to affect the surface layer that is developed underneath the traveling downburst eddies. However, in analogy to earlier experimental and numerical studies conducted at lower Reynolds numbers Re (Xu and Hangan, 2008 and Mason *et al.*, 2009), our investigation supports that surface roughness leads to a reduction of the observed maximum horizontal wind speed while simultaneously raising its height of occurrence above the ground. Contrary to the findings of Xu and Hangan (2008), the offset of the maximum velocity with respect to z_0 commences at the horizontal measurement location of overall maximum in the flow field. Furthermore, while the overall maximum velocity depends on Re and weakly on z_0 , its height of occurrence increases significantly for the largest z_0 tested and does not vary with Re . The time evolution of these two quantities suggests that, for $r \geq 1.2D$ with respect to the jet touchdown, the outgoing horizontal flow is retarded by increasing the surface roughness. This results from the formation of a recirculation bubble in front of the primary vortex (PV), named secondary vortex (SV), produced by the separation–reattachment of the boundary layer. Here, the slowdown of the PV enables the turbulence developed by the friction with the rough surface to influence the boundary layer height. The time development of the height of maximum velocity returns an idea of the boundary layer thickness, which increases along the radial direction by increasing z_0 due to the lifting of the interface between PV and SV. The surface layer height reduces when the SV is ejected from the PV surface and a re-equilibrium is achieved between wall friction and flow shear in the two layers. The analyses reveal a significant influence of surface roughness during the most intense stage of the downburst phenomenon, which could prove crucial in assessing wind loading and its effects on structures from a wind engineering perspective. In this context, relying on a static or quasi-static approach that assumes the stationarity of the downburst outflow and of the nose-shaped vertical profile shall turn out flawed. This study critically debates the experimental and numerical model of Xu and Hangan (2008). However, none of the experimental studies on downburst winds have approached the Re tested in our investigation which enabled to classify the produced flows in the fully turbulent regime and thus to extend the results to the full-scale environment. Particularly, the large Re testing allowed to properly characterize the boundary layer behavior and its separation from the rough surfaces, which is not necessarily observed at lower Re . Turbulence intensity is largely affected by the different grades of rough surfaces particularly at the near-ground level, where turbulence increases by increasing z_0 . A characteristic C and reversed-S-like shapes of turbulence vertical profiles are observed at $r/D = 1.0$ (location of overall maximum velocity) during the passage of the PV (most intense stage of the phenomenon) and following steady-velocity part, respectively.

The characterization of the effects of roughness length on the experimentally produced downburst outflows provides important insight into the formulation of a complete analytical model of thunderstorm winds to apply to the design of structures and infrastructures. The comparison and validation with full-scale measurements of downburst winds recorded in the Northern Mediterranean area (Canepa *et al.*, 2020; 2023a) will further significantly contribute to its success.

ACKNOWLEDGMENTS

The authors are deeply grateful to Giovanni Solari for his essential contributions to the conceptualization, supervision, and funding of this research.

This study was carried out within the RETURN Extended Partnership and received funding from the European Union Next-Generation EU (National Recovery and Resilience Plan – NRRP, Mission 4, Component 2, Investment 1.3 – D.D. 1243 2/8/2022, PE0000005). The first and second authors acknowledge the support of the European Research Council (ERC) under the European Union's Horizon 2020 research and innovation program (Grant Agreement No. 741273) for the project THUNDERR—Detection, simulation, modelling and loading of thunderstorm outflows to design wind-safer and cost-efficient structures—awarded with Advanced Grant No. 2016. Support from the Canada Foundation for Innovation (CFI) WindEEE Dome Grant (No. X2281B38) is also acknowledged.

AUTHOR DECLARATIONS

Conflict of Interest

The authors have no conflicts to disclose.

Author Contributions

Federico Canepa: Data curation (lead); Formal analysis (lead); Investigation (lead); Methodology (equal); Software (lead); Validation (lead); Visualization (lead); Writing – original draft (lead).
Massimiliano Burlando: Conceptualization (equal); Methodology (equal); Project administration (equal); Supervision (equal); Visualization (supporting); Writing – review & editing (equal).
Djordje Romanic: Conceptualization (equal); Data curation (supporting); Investigation (supporting); Methodology (equal); Software (supporting); Supervision (supporting); Writing – review & editing (equal).
Horia Hangan: Conceptualization (equal); Funding acquisition (supporting); Methodology (equal); Project administration (supporting); Resources (lead); Supervision (equal); Writing – review & editing (equal).

DATA AVAILABILITY

The data (instantaneous 3-component wind speed raw measurements) that support the findings of this study are openly available in the Zenodo repository at <https://doi.org/10.5281/zenodo.10686950> (Canepa et al., 2024). Instruction to read and re-use the dataset of measurements is provided at the same DOI.

REFERENCES

- Aboshosha, H., Bitsuamlak, G., and El Damatty, A., “Turbulence characterization of downbursts using LES,” *J. Wind Eng. Ind. Aerodyn.* **136**, 44–61 (2015).
- Byers, H. R. and Braham, R. R., “Thunderstorm structure and circulation,” *J. Meteorol.* **5**, 71–86 (1948).
- Canepa, F., Burlando, M., Hangan, H., and Romanic, D., “Experimental investigation of the near-surface flow dynamics in downburst-like impinging jets immersed in ABL-like winds,” *Atmosphere* **13**, 621 (2022a).
- Canepa, F., Burlando, M., and Repetto, M. P. (2023a), “Thunderstorm outflows in the Mediterranean Sea area,” Zenodo. <https://doi.org/10.5281/zenodo.7495115>
- Canepa, F., Burlando, M., Romanic, D., and Hangan, H. (2024), “Experimental measurements of the effects of surface roughness on large-scale downburst-like impinging jets at the WindEEE Dome laboratory,” Zenodo. <https://doi.org/10.5281/zenodo.10686950>
- Canepa, F., Burlando, M., Romanic, D., Solari, G., and Hangan, H., “Experimental investigation of the near-surface flow dynamics in downburst-like impinging jets,” *Environ. Fluid Mech.* **22**, 921 (2022b).
- Canepa, F., Burlando, M., Romanic, D., Solari, G., and Hangan, H., “Downburst-like experimental impinging jet measurements at the WindEEE Dome,” *Sci. Data* **9**, 243 (2022c).
- Canepa, F., Burlando, M., and Solari, G., “Vertical profile characteristics of thunderstorm outflows,” *J. Wind Eng. Ind. Aerodyn.* **206**, 104332 (2020).
- Canepa, F., Romanic, D., Hangan, H., and Burlando, M., “Experimental translating downbursts immersed in the atmospheric boundary layer,” *J. Wind Eng. Ind. Aerodyn.* **243**, 105570 (2023b).
- Davenport, A. G., *The Relationship of Wind Structure to Wind Loading* (National Physical Laboratory, 1963).
- De Bruin, H. A. R. and Moore, C. J., “Zero-plane displacement and roughness length for tall vegetation, derived from a simple mass conservation hypothesis,” *Boundary-Layer Meteorol.* **31**, 39–49 (1985).
- ESDU 82026, “Strong winds in the atmospheric boundary layer. Part 1: Hourly-mean wind speeds,” 2002.
- Farshad, F., Rieke, H., and Garber, J., “New developments in surface roughness measurements, characterization, and modeling fluid flow in pipe,” *J. Pet. Sci. Eng.* **29**, 139–150 (2001).
- Fujita, T. T., *Andrews AFB Microburst*, SMRP Research Paper 205 (University of Chicago, 1983).
- Fujita, T. T., *The Downburst - Microburst and Macroburst - Report of Projects NIMROD and JAWS* (University of Chicago, 1985).
- Gairola, A., Bitsuamlak, G. T., and Hangan, H. M., “An investigation of the effect of surface roughness on the mean flow properties of “tornado-like” vortices using large eddy simulations,” *J. Wind Eng. Ind. Aerodyn.* **234**, 105348 (2023).
- Hangan, H., “The wind engineering energy and environment (WindEEE) Dome at Western University, Canada,” *Wind Eng. JAWE* **39**, 350–351 (2014).
- Hangan, H., Refan, M., Jubayer, C., Romanic, D., Parvu, D., LoTufo, J., and Costache, A., “Novel techniques in wind engineering,” *J. Wind Eng. Ind. Aerodyn.* **171**, 12–33 (2017).
- Hjelmfelt, M. R., “Structure and life cycle of microburst outflows observed in Colorado,” *J. Appl. Meteorol.* **27**, 900–927 (1988).
- Junayed, C., Jubayer, C., Parvu, D., Romanic, D., and Hangan, H., “Flow field dynamics of large-scale experimentally produced downburst flows,” *J. Wind Eng. Ind. Aerodyn.* **188**, 61–79 (2019).
- Konina, K., Kruszelnicki, J., Meyer, M. E., and Kushner, M. J., “Surface ionization waves propagating over non-planar substrates: Wavy surfaces, cut-pores and droplets,” *Plasma Sources Sci. Technol.* **31**, 115001 (2022).
- Lettau, H., “Note on aerodynamic roughness-parameter estimation on the basis of roughness-element description,” *J. Appl. Meteorol.* **8**, 828–832 (1969).
- Mason, M. S., Wood, G. S., and Fletcher, D. F., “Influence of tilt and surface roughness on the outflow wind field of an impinging jet,” *Wind Struct.* **12**, 179–204 (2009).
- Meyer, M., Foster, J., and Kushner, M. J., “A surface mechanism for O₃ production with N₂ addition in dielectric barrier discharges,” *Plasma Sources Sci. Technol.* **32**, 085001 (2023).
- Popiel, C. O. and Trass, O., “Visualization of a free and impinging round jet,” *Exp. Therm. Fluid Sci.* **4**, 253–264 (1991).
- Romanic, D. and Hangan, H., “Experimental investigation of the interaction between near-surface atmospheric boundary layer winds and downburst outflows,” *J. Wind Eng. Ind. Aerodyn.* **205**, 104323 (2020).
- Romanic, D., Nicolini, E., Hangan, H., Burlando, M., and Solari, G., “A novel approach to scaling experimentally produced downburst-like impinging jet outflows,” *J. Wind Eng. Ind. Aerodyn.* **196**, 104025 (2020).
- Solari, G., Burlando, M., De Gaetano, P., and Repetto, M. P., “Characteristics of thunderstorms relevant to the wind loading of structures,” *Wind Struct.* **20**, 763–791 (2015).
- Stearns, C. R., “Determining surface roughness and displacement height,” *Boundary-Layer Meteorol.* **1**, 102–111 (1970).
- Vermeire, B. C., Orf, L. G., and Savory, E., “Improved modelling of downburst outflows for wind engineering applications using a cooling source approach,” *J. Wind Eng. Ind. Aerodyn.* **99**, 801–814 (2011).
- White, F. M., *Viscous Fluid Flow*, 2nd ed. (McGraw-Hill, 1991).
- Xu, Z. and Hangan, H., “Scale, boundary and inlet condition effects on impinging jets,” *J. Wind Eng. Ind. Aerodyn.* **96**, 2383–2402 (2008).